Chalcogenide Letters

Tech Science Press

http://doi.org/10.32604/cl.2026.080386

ARTICLE

First-Principles Insights into the Structural and Physical Properties of $AgSbS_2$

Tianjing Li[1,*], Min Yao[1], Wei Li[1], Yue Yang[1], Luping Qu[1], Haijun Hou[2] and Hongli Guo[3]

[1]Institute of Automotive and Traffic Engineering, Yancheng Polytechnic College, Yancheng, China
[2]School of Materials Engineering, Yancheng Institute of Technology, Yancheng, China
[3]College of Electronic and Information Engineering, Yangtze Normal University, Fuling, Chongqing, China
*Corresponding Author: Tianjing Li. Email: litj1021@126.com

Received: 08 February 2026; Accepted: 03 May 2026; Published: 02 June 2026

ABSTRACT: This study focuses on monoclinic system $AgSbS_2$, employing first-principles methods to calculate the structural, mechanical, optical, and thermodynamic properties. Specifically, geometry optimization yields a stable atomic structure with optimized lattice constants (a = 12.82 Å, b = 4.41 Å, and c = 13.19 Å). Furthermore, electronic structure analysis identifies $AgSbS_2$ as a direct bandgap semiconductor with a bandgap of 1.456 eV, where the valence and conduction bands primarily originate from Ag-4d, S-3s, and Sb-5p states. Regarding the elastic properties, the calculated elastic constants, combined with Pugh's B/G criterion, reveal excellent ductility. As for the optical properties, the static dielectric constant $\varepsilon_1(0)$ is 8.25 and the static refractive index n_0 is 2.87. The maximum absorption occurs at a photon energy of approximately 6.62 eV, the maximum reflectivity at about 9.33 eV, and maximum energy loss at 12.17 eV. Finally, the thermodynamic properties are systematically evaluated.

KEYWORDS: $AgSbS_2$; electronic structure; elastic properties; thermal properties

1 Introduction

$AgSbS_2$ is a ternary p-type semiconductor inorganic photovoltaic material belonging to the I-V-VI_2 group. Its unique layered structure endows optoelectronic devices with excellent absorption performance [1,2]. Abundant, environmentally friendly and non-toxic, $AgSbS_2$ holds great potential for enhancing visible light absorption and improving the photoelectric conversion efficiency of photovoltaic devices [3]. $AgSbS_2$ exhibits outstanding photoelectric properties. Firstly, making it suitable for solar cell fabrication [4]. Moreover, the bandgap can be adjusted through elemental doping and selenization to optimize the performance of thin films and corresponding devices. Secondly, $AgSbS_2$ has a high absorption coefficient, enabling it to absorb a large amount of sunlight in thin absorption layers, thereby reducing device fabrication costs, improving material utilization, and promoting commercialization [5]. As early as 1995, Ibrahim's research group [6] conducted preliminary studies on $AgSbS_2$, preparing $AgSbS_2$ thin films and investigating the structure, and physical properties of $AgSbS_2$ thin films. Choi et al. studied the surface ligand interactions of $AgSbS_2$ quantum dots synthesized with 1-dodecanethiol used as a stabilizer [7]. Recently, Dutkova et al. have successfully synthesized a ternary $AgSbS_2$ semiconductor through a one-step mechanical chemical synthesis method using elemental silver, antimony and sulfur as raw materials, after grinding [8]. In addition, Oubakalla et al. reported the fabrication of a novel $AgSbS_2$ electrode via electrodeposition onto fluorine-doped tin oxide (FTO) substrates and systematically compared its supercapacitive performance in lithium-containing aqueous versus organic electrolytes [9]. Mohanty et al. report the preparation and systematic investigation of structural, optical, and compositional properties of $Ag_{25-x}S_{35}Se_{40}Sb_x$ (x = 0, 5, 10, 15, 20 at%) quaternary chalcogenide thin films [10]. On the theoretical side, Hosni et al. [11] conducted a detailed study on the electronic properties of $AgSbS_2$ based on density functional theory calculations. Although experiments and some theories have been conducted on $AgSbS_2$, the optical and thermodynamic properties of the system have not been reported. This paper has conducted a detailed study on the optical and thermodynamic properties of the material, hoping that our research can provide some assistance for experimental studies.

2 Computational Methods

Geometric optimization calculations were performed in the CASTEP code [12–15]. For the geometric structure optimization of $AgSbS_2$, the ultrasoft pseudopotential was selected, the GGA-PBE exchange-correlation energy was adopted [16,17], and the cutoff energy was set to 400 eV. After comprehensive consideration, the *k*-point grid was set to 5 × 5 × 5. The valence electron configurations of the atoms were chosen as follows: Ag: $4d^{10}5s^1$, Sb: $5s^25p^3$, and S: $3s^23p^4$.

3 Results and Discussion

3.1 Structural Optimization

$AgSbS_2$ belong to the pyrargyrite type, crystallizing in the monoclinic system with a point group of 2/m and a space group of C2/c (Fig. 1). A crystal model was constructed, with lattice constants set to a = 12.72 Å, b = 4.27 Å, and c = 13.19 Å [18]. In the crystal, the model contains 32 atoms, Ag atoms occupy 4e and 4b Wyckoff positions, whereas Sb and S occupy 8f Wyckoff position. The structural parameters of $AgSbS_2$ are listed in Table 1. The optimized result we obtained is consistent with the other values [18,19], indicating that our calculation is reliable.

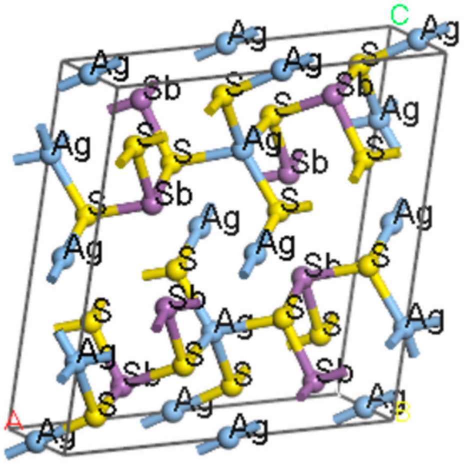

Figure 1: Unit cell of $AgSbS_2$.

Table 1: Lattice constant of $AgSbS_2$.

	a **(Å)**	***b*** **(Å)**	***c*** **(Å)**	$\boldsymbol{\beta}^{\circ}$ **(°)**
Present	12.82	4.41	13.19	99.57
Ref. [18]	12.72	4.27	13.12	
Exp. [19]	12.862	4.409	13.218	98.48

3.2 Electronic Structure

Fig. 2 shows the energy band structure of $AgSbS_2$, with a band gap (E_g) of 1.456 eV. From the energy band diagram, the valence band maximum (VBM) and the conduction band minimum (CBM) are not on the same line, indicating that $AgSbS_2$ is a direct bandgap semiconductor.

$$E_g = E_{CBM} - E_{VBM} \tag{1}$$

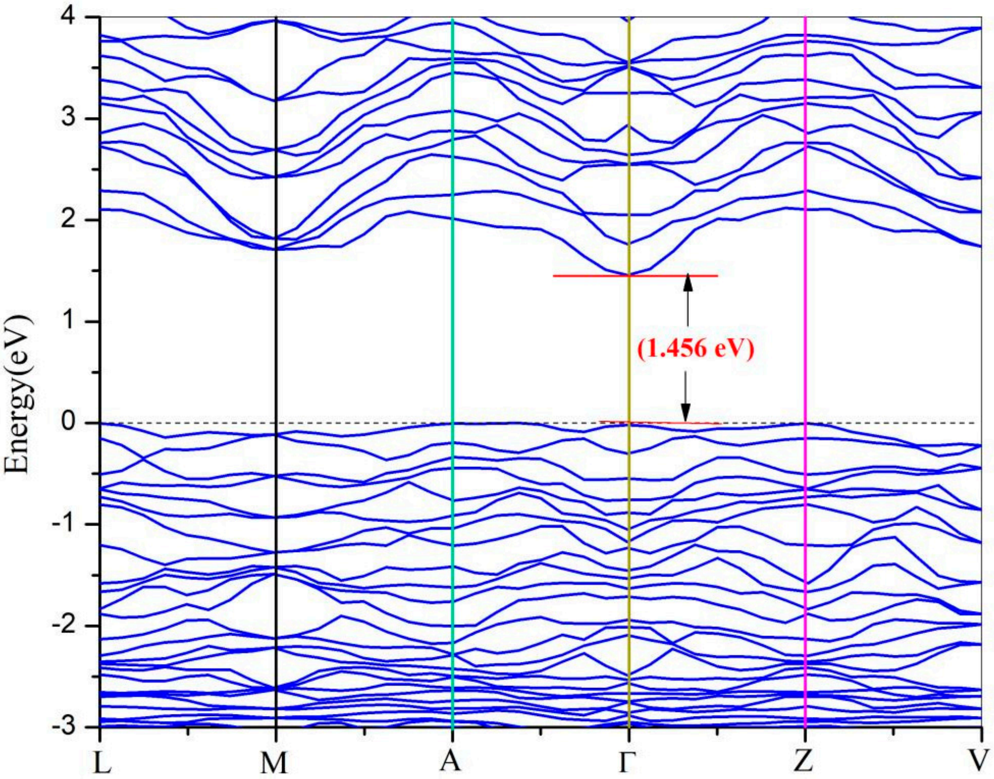

Figure 2: Band structure of $AgSbS_2$.

Fig. 3 presents the density of states of $AgSbS_2$ obtained using the GGA method. Analysis of the data in Fig. 3 reveals the detailed characteristics of the valence band structure of $AgSbS_2$, which exhibits a distinct layered distribution consisting of three band components. The lower valence band shows a significant peak in the electron density of states at a photon energy of −12.1 eV, indicating that S-3s and Sb-5p contribute to the total density of states in the energy range of −14.2 eV to −11.2 eV, with hybridization of the Sb-5s orbital, resulting in obvious electron localization. The middle valence band has a distribution peak at −8.75 eV, indicating that Sb-5s and S-3p dominate in the range of −9.45 eV to −6.88 eV, with a small contribution from the S-3s orbital, further enhancing electron localization. The upper valence band spans the energy −5.63 eV to 0 eV, with two peaks at −2.91 eV and −0.756 eV. The former is formed by the combined action of the Ag-4d, S-3p, and Sb-5p, accompanied by the participation of a small amount of the Sb-5s orbital; the latter is formed by the combined action of the S-3p and Sb-5p orbitals, with hybridization of the Ag-4d and Sb-5s. As shown in Fig. 3, the VBM is mainly composed of S-3p and Ag-4d, while the CBM mainly relies on the Sb-5p orbital, with a small contribution from the Ag-4d orbital.

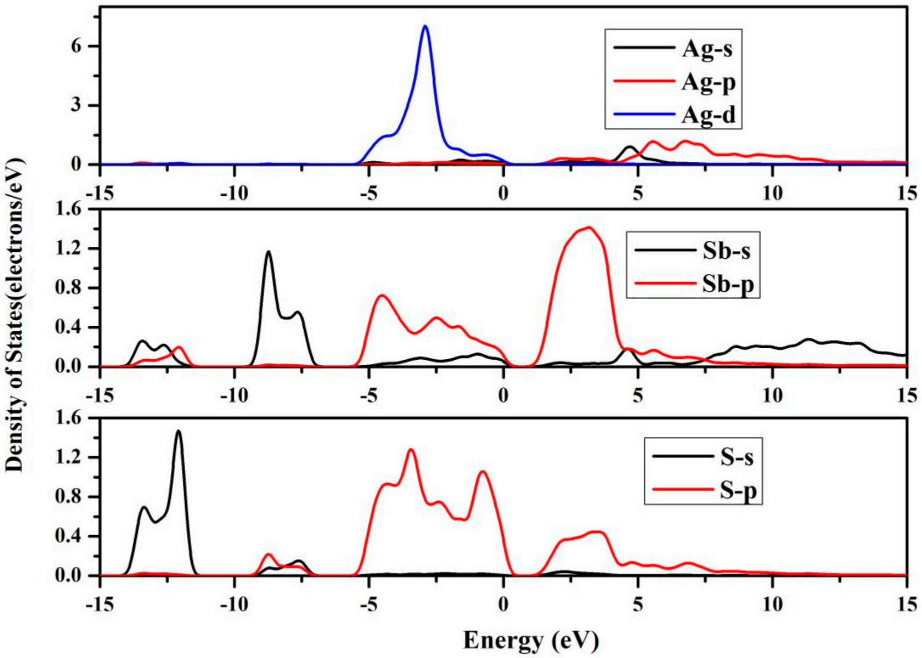

Figure 3: Density of states of $AgSbS_2$.

3.3 Elastic Properties

Elastic constants (C_{ij}) characterize a crystal's resistance to elastic deformation, reflect interatomic bond stiffness and lattice mechanical stability, and serve as the basis for calculating bulk modulus, shear modulus and other mechanical parameters, as well as for judging mechanical anisotropy and structural stability. The data in Table 2 indicates that for the monoclinic structure, $AgSbS_2$ possess thirteen independent elastic constants (C_{ij}). To assess its mechanical stability, the C_{ij} values of $AgSbS_2$ were determined according to Ref. [20]. The results (Table 2) fulfilled all necessary stability criteria, confirming that the material is mechanically stable.

Table 2: Elastic constants C_{ij} (GPa) of $AgSbS_2$ at 0–40 GPa.

Pressure (GPa)	**0**	**10**	**20**	**30**	**40**
C_{11}	55.88	113.37	140.25	152.92	182.06
C_{22}	23.24	174.67	231.76	307.51	366.25
C_{33}	52.22	179.25	238.22	304.89	372.01
C_{44}	16.61	45.78	57.76	73.67	87.58
C_{55}	17.32	47.96	72.05	110.47	142.64
C_{66}	14.61	43.81	69.84	116.06	145.79
C_{12}	18.08	97.13	137.24	174.94	214.75
C_{13}	26.11	98.55	137.85	173.44	211.18
C_{15}	−3.26	0.86	1.22	6.39	5.25
C_{23}	16.80	88.85	122.60	161.56	195.23
C_{25}	0.85	−23.38	−36.97	−43.74	−30.92
C_{35}	−1.80	24.03	35.07	37.56	20.65
C_{46}	−0.53	−22.07	−34.28	−41.15	−27.79

In Table 3, the bulk modulus B and shear modulus G of $AgSbS_2$ gradually increases with increasing pressure. The Poisson's ratio v can determine the material's resistance to shear deformation; typically, a Poisson's ratio between −1 and 0.5 indicates relative stability against shear deformation. The Poisson's ratio of $AgSbS_2$ ranges from 0.2 to 0.4, indicating that the higher the pressure, the better the plasticity. The ductility of a material is represented by B/G. Pugh's B/G criterion [21] is a widely used method to evaluate material ductility: A material is deemed ductile if the B/G ratio surpasses 1.75; otherwise, it exhibits brittle behavior. As shown in the table, the B/G value of $AgSbS_2$ is much greater than 1.75, confirming that the crystal has excellent ductility and is suitable for mechanical processing. This ductility provides strong support for the application of $AgSbS_2$ in precision manufacturing.

Table 3: Calculated B (GPa), G (GPa), young's modulus E (GPa), B/G and Poisson's ratio ν of $AgSbS_2$ at 0–40 GPa.

Pressure (GPa)	***B***	***G***	***E***	***B/G***	***ν***
0	25.08	13.49	34.32	1.85	0.27
10	111.87	33.63	91.71	3.32	0.36
20	148.12	41.94	114.98	3.53	0.37
30	168.88	53.12	144.25	3.17	0.35
40	197.76	62.80	170.39	3.14	0.35

3.4 Optical Properties

The optical properties of the crystal are determined by the dielectric function $\varepsilon(\omega)$ given by $\varepsilon(\omega) = \varepsilon_1(\omega) + i\varepsilon_2(\omega)$. The imaginary part of $\varepsilon_2(\omega)$ depends on the joint density of states and the momentum matrix elements. The real part $\varepsilon_1(\omega)$ was obtained from $\varepsilon_2(\omega)$ by the Kramers-Kronig relations [22,23]:

$$\varepsilon_1(\omega) = \varepsilon_\infty + \frac{2}{\pi} p \int_0^\infty \frac{\omega' \varepsilon_2(\omega')}{\omega'^2 - \omega^2} d\omega' \tag{2}$$

$$\varepsilon_2(\omega) = -\frac{2\omega}{\pi} p \int_0^\infty \frac{\varepsilon_2(\omega') - \varepsilon_\infty}{\omega'^2 - \omega^2} d\omega' \tag{3}$$

ε_∞: High-frequency dielectric constant, ω: Angular frequency of incident light, ω': Integral variable (angular frequency), P: Cauchy principal value integral (avoiding integral singularities and ensuring integral convergence).

Fig. 4 shows the evolution law of the dielectric function. The static dielectric constant $\varepsilon_1(0)$ of the material is 8.25. Notably, the imaginary part ε_2 exhibits a steep increase in the low-energy region, reaching a peak of 12.15 when the photon energy is 3.67 eV, followed by an attenuation in the higher energy region, gradually approaching zero after the energy reaches 10.39 eV. The variation curve of the real part ε_1 rises to a maximum of 12.15 at 2.15 eV, then drops sharply to the negative region of −5.03 at 6.0 eV, and then gradually recovers to a gentle upward trend.

As can be seen from Fig. 5, the static refractive index n_0 of $AgSbS_2$ is 2.87. In the low-energy regime, the refractive index n rises monotonically with photon energy, attains a maximum value of 3.57 at 2.41 eV, and subsequently declines steeply as the photon energy further increases. It is worth noting that the peak distribution of the extinction coefficient k is plotted in Fig. 4, and its overall variation trend is similar to that of the imaginary part ε_2. In contrast, the extinction coefficient k peaks at 2.37 when the photon energy is 4.67 eV.

Fig. 6 shows the calculated absorption coefficient α. When the photon energy < 0.67 eV, α is almost zero. When the photon energy is greater than 0.67 eV, α increases sharply, reaching a maximum absorption peak of 2.11×10^5 cm^{-1} at approximately 6.62 eV, and then decreases with increasing energy, eventually approaching zero.

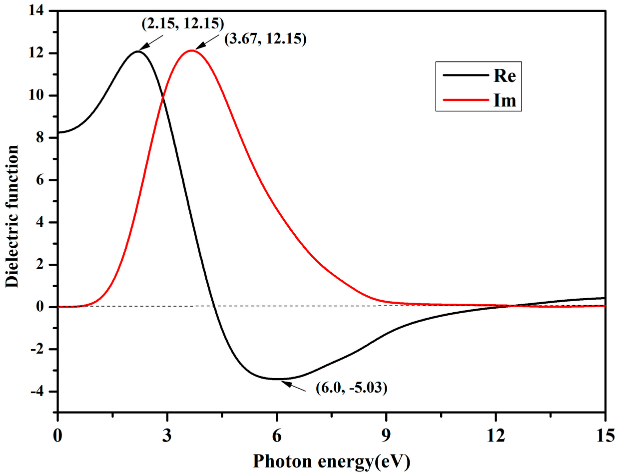

Figure 4: Dielectric function of $AgSbS_2$.

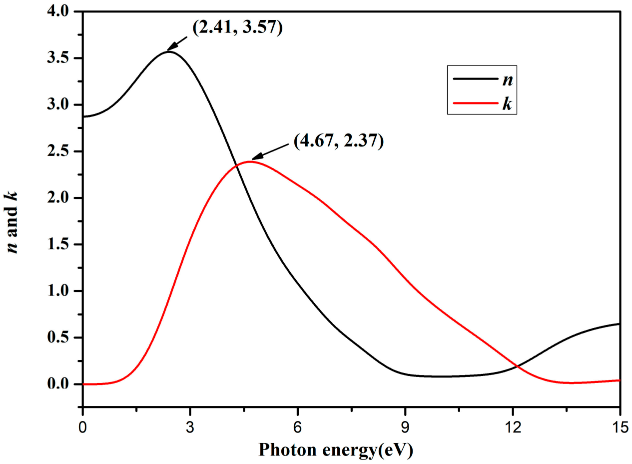

Figure 5: Refractive index and extinction coefficient of $AgSbS_2$.

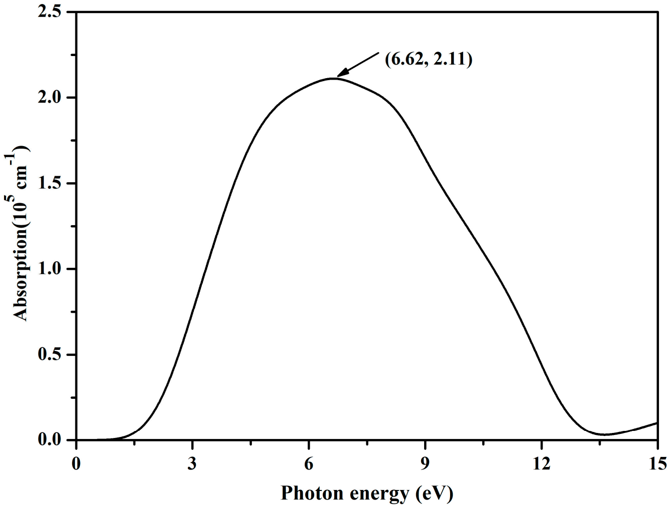

Figure 6: Absorption coefficient of $AgSbS_2$.

Fig. 7 shows the reflectivity calculation results. The static reflectivity $R(0)$ of $AgSbS_2$ material is 0.23. Notably, as the photon energy rises to 9.33 eV, the reflectivity peaks at 84%, which is the maximum value in the entire energy range.

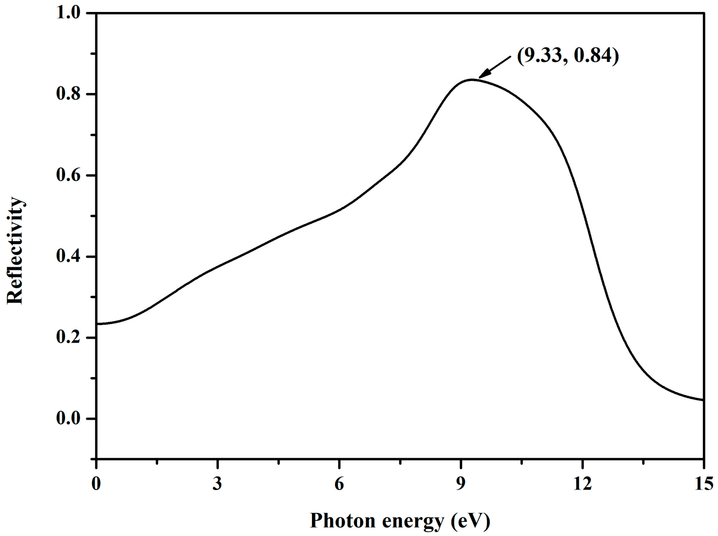

Figure 7: Reflectivity of $AgSbS_2$.

Fig. 8 shows the calculated conductivity. In the energy range of 0 eV~0.77 eV, the real part of the conductivity is zero. This phenomenon is due to the bandgap of $AgSbS_2$ being 1.456 eV; electrons with photon energy lower than this cannot be endowed with sufficient energy to achieve transition. As the photon energy rises to 4.14 eV, the real part reaches a maximum of 5.73 $(fs)^{-1}$. Finally, with the increase of photon energy, the real part of the conductivity continues to decrease and gradually approaches zero.

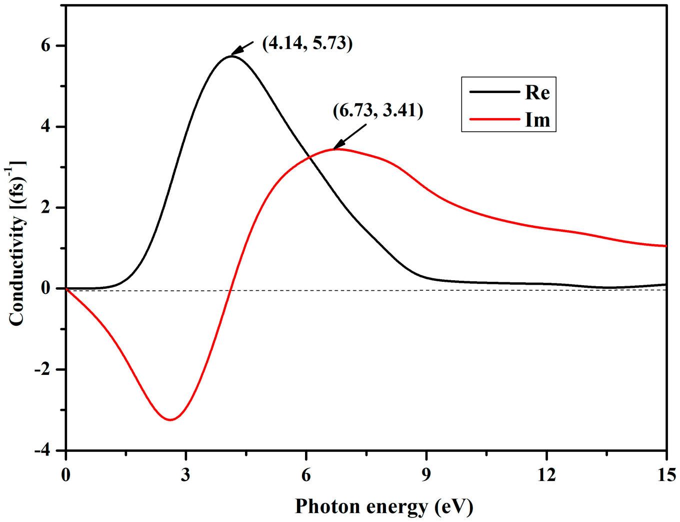

Figure 8: Conductivity of $AgSbS_2$.

Fig. 9 shows the calculated loss function. There is a resonance peak; when the photon energy is 12.17 eV, the energy loss of $AgSbS_2$ reaches a maximum, and then drops sharply to zero.

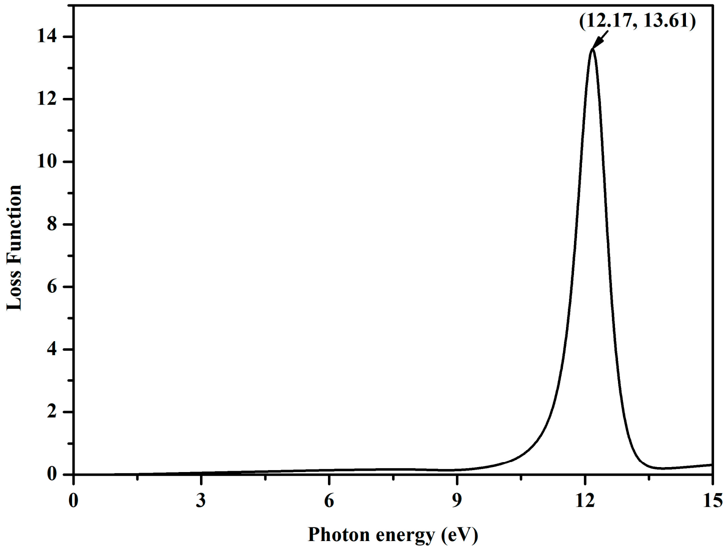

Figure 9: Energy loss function of $AgSbS_2$.

3.5 Thermal Properties

We obtained the total energy E and volume V of the primitive cell through energy calculations, and fitted E-V curve according to the Murnaghan equation [24], as shown in Fig. 10. The thermal properties of $AgSbS_2$ under high pressure and high temperature, we have used the quasi-harmonic Debye model as implemented in the Gibbs code [25].

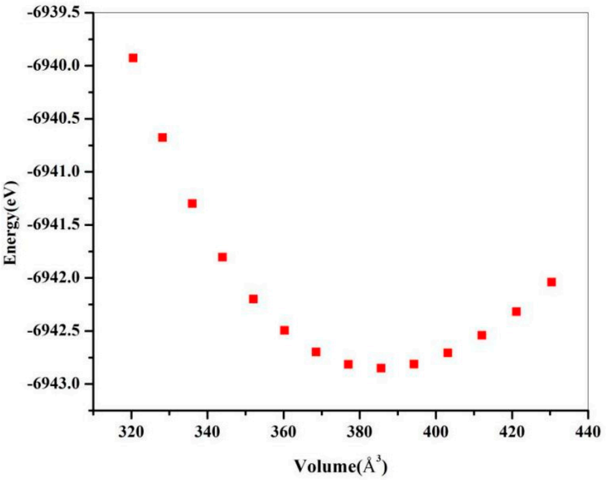

Figure 10: Relationship between E and V.

Fig. 11 shows the relationship between B and T under $P = 0$: when $T < 100$ K, the value of B is basically stable; when $T > 100$ K, B decreases linearly with increasing temperature.

Fig. 12 presents the variation curves of B with P in the range of 0~15 GPa when T is 0 K, 500 K, and 1000 K: under isothermal conditions, B increases with increasing pressure; under isobaric conditions, B decreases with increasing temperature. Increasing pressure or decreasing temperature can produce similar changes in the bulk modulus of the material.

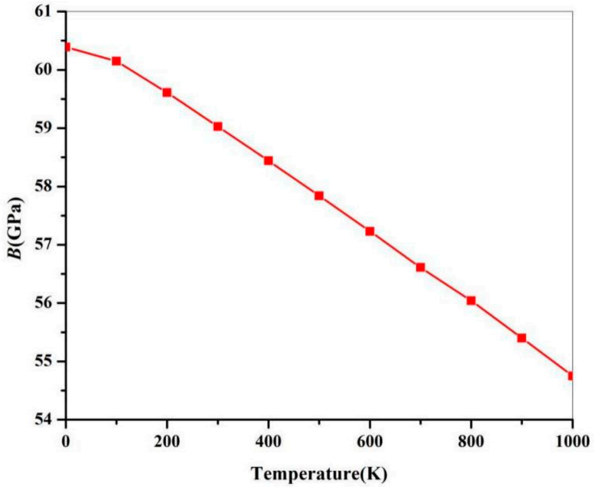

Figure 11: Variation of *B* with *T* at $P = 0$.

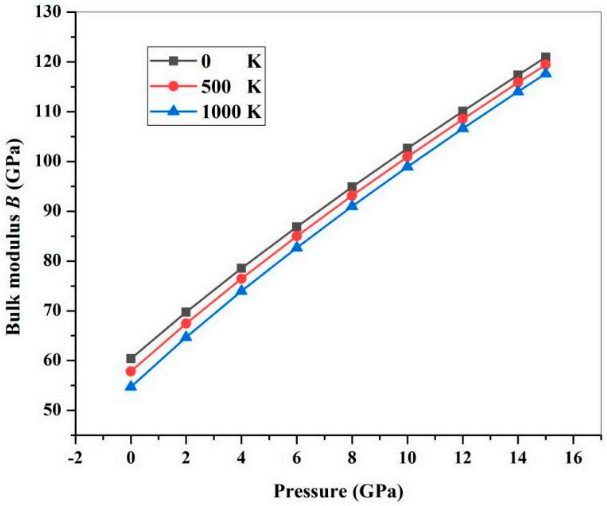

Figure 12: Variation of *B* with *P* at different temperatures.

Table 4 shows the Entropy *S*, Grüneisen parameter γ, and Debye temperature θ obtained under different temperatures and pressures. At the same pressure, *S* and γ increase with increasing temperature *T*, and decrease with increasing temperature; at the same temperature, θ increases with increasing pressure *P*, while *S* and γ decrease with increasing pressure. When the pressure increases, the decline in *S* occurs more rapidly at lower temperatures than at higher ones, moreover, the rate of rise in θ accelerates at elevated temperatures compared to that observed at lower temperatures, and the decrease rate of γ at high temperatures is faster. Overall, the γ value ranges from 1.6 to 2.3, indicating that $AgSbS_2$ has moderate thermal expansion. As the *P* rises from 0 GPa to 15 GPa, the entropy *S* decreases by 43.85%, the Debye temperature θ increases by 37.73%, and the Grüneisen constant γ decreases by 28.67%, at 100 K, the entropy *S* decreases by 19.52%, the Debye temperature θ increases by 38.73%, and the Grüneisen constant γ decreases by 29.07% at 400 K, the entropy *S* decreases by 15.25%, the Debye temperature θ increases by 39.86%, and the Grüneisen constant γ decreases by 29.69% at 700 K, the entropy *S* decreases by 13.47%, the Debye temperature θ increases by 41.07%, and the Grüneisen constant γ decreases by 30.17% at 1000 K, respectively.

Table 4: S (J·mol^{-1}·K^{-1}), θ (K), and γ of $AgSbS_2$ at different temperatures and pressures.

***T*/K**	***P*/GPa**	**0**	**4**	**8**	**12**	**15**
100	S	40.47	33.00	28.19	24.74	22.72
	θ	310.99	351.51	383.48	410.47	428.35
	γ	2.243	1.98	1.80	1.68	1.600
400	S	160.59	148.42	139.88	133.33	129.25
	θ	307.94	349.34	381.95	409.17	427.21
	γ	2.27	1.99	1.81	1.68	1.61
700	S	216.57	203.70	194.71	187.83	183.54
	θ	304.47	346.86	380.04	407.62	425.83
	γ	2.29	2.01	1.82	1.69	1.61
1000	S	253.09	239.70	230.44	223.37	218.99
	θ	300.87	344.32	378.07	406.04	424.43
	γ	2.32	2.02	1.83	1.70	1.62

Fig. 13 illustrates how the heat capacity C_V varies with T. At the same pressure, as the temperature changes from low to high, C_V gradually increases. In the low-temperature region (0~200 K), C_V shows a strong increasing trend, which is because acoustic phonons mainly contribute to the heat capacity at low temperatures. With increasing temperature, the growth rate of isochoric specific heat accelerates, which is due to the gradual excitation of optical phonons and their increasing contribution to the C_V. With the continuous increase of temperature T and pressure P, the C_V gradually stabilizes, approaching the Dulong-Petit limit value.

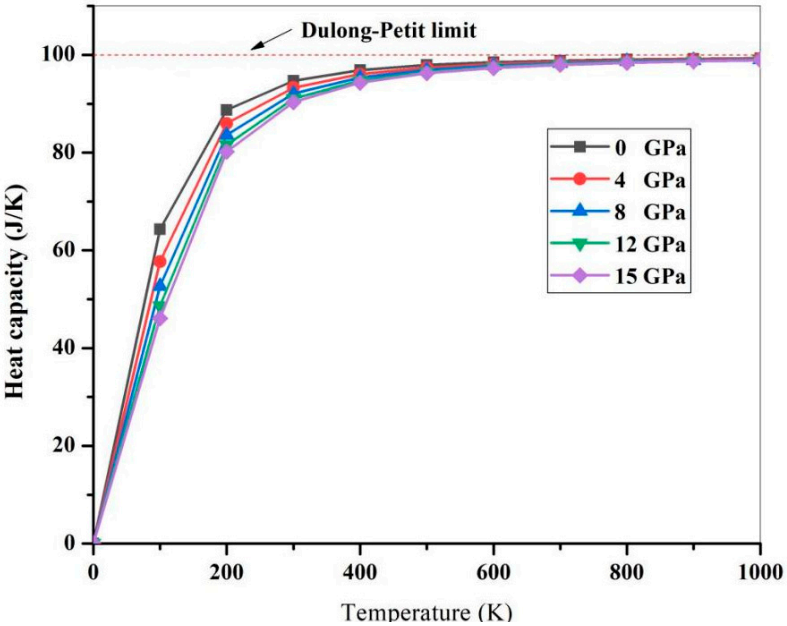

Figure 13: Variation of C_V with T under different pressures.

Fig. 14 shows the relationship between α and T. Over the T interval from 0 K to 1000 K, the thermal expansion coefficient gradually increases with increasing temperature. In $T < 300$ K, the α is small; with increasing temperature, α increases significantly, which is because the atomic vibration intensifies and the average distance between atoms increases, leading to the expansion of the unit cell volume. Beyond 300 K, the parameter α exhibits a gradual linear rise. Notably, the increase in pressure will weaken the rate of change of α with temperature, especially in the high-temperature region, where α is almost unaffected by temperature fluctuations.

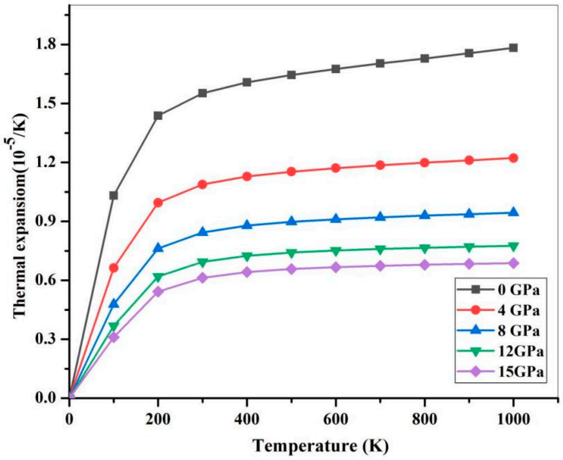

Figure 14: Variation of α with T under different pressures.

Fig. 15 shows the relationship between α and P. The curves under various temperature conditions all show that α decreases with increasing pressure P. At $P > 15$ GPa, the α value at high temperatures approaches and stabilizes, indicating that under high temperature and high pressure, α is basically unaffected by temperature T and pressure P. The increase in pressure causes the lattice to deform, shortening the equilibrium distance between atoms and prompting them to move into more repulsive regions of the interatomic potential energy curve. This makes the potential energy well more robust, inhibiting its inherent asymmetry (which is the fundamental cause of thermal expansion), and limiting the amplitude of atomic thermal vibrations during heating. Overall, these effects weaken the overall increase in average atomic spacing, thereby reducing the phenomenon of thermal expansion.

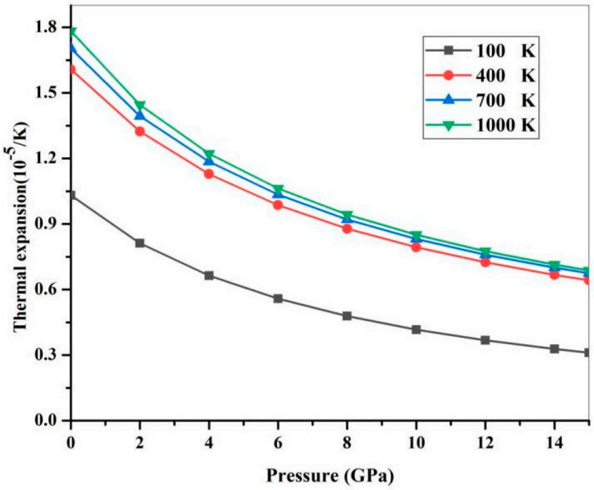

Figure 15: Variation of α with P at different temperatures.

4 Conclusions

Based on first-principles calculations, this study systematically investigates the physical properties of monoclinic $AgSbS_2$. The optimized structural parameters are consistent with previous theoretical values. Electronic structure analysis reveals a direct bandgap of 1.456 eV, and the density of states indicates that the valence and conduction bands mainly originate from the hybridisation of Ag-4d, S-3s, and Sb-5p states. From the calculated elastic constants C_j, key mechanical parameters (B, G, E and v) are derived. The B/G ratio exceeds 1.75, confirming that $AgSbS_2$ is an excellent ductile material. The optical properties are also calculated and analysed. Finally, the pressure and temperature dependencies of the heat capacity, entropy, Grüneisen parameter, thermal expansion coefficient, and Debye temperature are systematically obtained.

Acknowledgement: Not applicable.

Funding Statement: This research was funded by the Technology Innovation Team of Yancheng Polytechnic College (YGKJ202503).

Author Contributions: The authors confirm contribution to the paper as follows: study conception and design: Tianjing Li; data collection: Tianjing Li; analysis and interpretation of results: Yue Yang; draft manuscript preparation: Tianjing Li, Min Yao, Wei Li, Yue Yang, Luping Qu, Haijun Hou, Hongli Guo. All authors reviewed and approved the final version of the manuscript.

Availability of Data and Materials: Not applicable.

Ethics Approval: Not applicable.

Conflicts of Interest: The authors declare no conflicts of interest.

References

1. Capistrán-Martínez J, Nair PK. Photoconductive thin films of $AgSbS_2$ with cubic crystalline structure in solar cells. Phys Status Solidi A. 2015;212(12):2869–76. [CrossRef].
2. Chalapathi U, Reddy AS, Prasad PR, Manjula G, Sangaraju S, Cheruku R, et al. Two-stage-processed $AgSbS_2$ films for thin-film solar cells. Mater Sci Semicond Process. 2023;168:107821. [CrossRef].
3. Senina A, Prudnikau A, Wrzesińska-Lashkova A, Brunner J, Qi X, Shilovskikh VV, et al. Low-temperature synthesis and postsynthetic size-tunability of $AgSbS_2$ nanocrystals and their application in planar solar cells. ACS Appl Energy Mater. 2026;9(4):2067–79. [CrossRef].
4. Gu Y, Liang W, Wang H, Chen T. Hydrothermal deposition and further simulative optimization of device achieving efficiency close 19% for $AgSbS_2$ solar cell. Small. 2025;21(34):2504888. [CrossRef].
5. Zhang L, Zhu C, Chen T. Solution processed $AgSbS_2$ film for efficient planar heterojunction solar cells. Appl Phys Lett. 2021;119(15):151906. [CrossRef].
6. Ibrahim AM. Optical properties of ternary $AgSbS_2$ thin films. J Phys Condens Matter. 1995;7(29):5931–8. [CrossRef].
7. Choi H, Kim S, Luther JM, Kim SW, Shin D, Beard MC, et al. Facet-specific ligand interactions on ternary $AgSbS_2$ colloidal quantum dots. Chem A Eur J. 2017;23(70):17707–13. [CrossRef].
8. Dutková E, Baláž M, Kováč J, Sayagués MJ, Wohlgemuth M, Lukáčová Bujňáková Z, et al. Rapid one-step mechanochemical synthesis of ternary semiconductor $AgSbS_2$ for photovoltaic applications. J Mater Sci. 2025;60(33):14605–20. [CrossRef].
9. Oubakalla M, Zimou J, Nejmi Y, El Bouji M, Fareh K, Beraich M, et al. Development of a new electrodeposited $AgSbS_2$/FTO electrode: Comparison of supercapacitance in Li-based aqueous and organic electrolytes. Mater Chem Phys. 2024;314:128867. [CrossRef].
10. Mohanty B, Alagarasan D, Naik R. Enhancement in electrical conductivity and hydrophobicity in $Ag_{25-x}S_{35}Se_{40}Sb_x$ thin films by Sb doping for optoelectronic applications. Appl Phys A. 2025;131(8):608. [CrossRef].

11. Hosni N, Bouaniza N, Selmi W, Assili K, Maghraoui-Meherzi H. Synthesis and physico-chemical investigations of $AgSbS_2$ thin films using Doehlert design and under DFT framework. J Alloys Compd. 2019;778:913–23. [CrossRef].
12. Li TJ, Yue Y, Qu LP, Hou HJ, Fan SH, Guo HL, et al. Theoretical exploration of the structure and physical properties of $AgAlSe_2$. Chalcogenide Lett. 2025;22(10):917–27. [CrossRef].
13. Clark SJ, Segall MD, Pickard CJ, Hasnip PJ, Probert MIJ, Refson K, et al. First principles methods using CASTEP. Z Für Kristallogr Cryst Mater. 2005;220(5–6):567–70. [CrossRef].
14. Li TJ, Yue Y, Qu LP, Hou HJ, Fan SH, Guo HL. Electronic structure, optical properties, and elastic properties of solar material $CuInSe_2$ from theoretical simulation. Chalcogenide Lett. 2025;22(6):529–40. [CrossRef].
15. Segall MD, Lindan PJD, Probert MJ, Pickard CJ, Hasnip PJ, Clark SJ, et al. First-principles simulation: Ideas, illustrations and the CASTEP code. J Phys Condens Matter. 2002;14(11):2717–44. [CrossRef].
16. Perdew J, Burke K, Ernzerhof M. Generalized gradient approximation made simple. Phys Rev Lett. 1996;77(18):3865–8. [CrossRef].
17. Vanderbilt D. Soft self-consistent pseudopotentials in a generalized eigenvalue formalism. Phys Rev B. 1990;41(11):7892–5. [CrossRef].
18. Nadukkandy A, Devasia S, Abraham P, Shaji S, Avellaneda DA, Aguilar-Martínez JA, et al. Monoclinic $AgSbS_2$ thin films for photovoltaic applications: Computation, growth and characterization approaches. Mater Sci Semicond Process. 2021;135:106074. [CrossRef].
19. Effenberger H, Paar WH, Topa D, Criddle AJ, Fleck M. The new mineral baumstarkite and a structural reinvestigation of aramayoite and miargyrite. Am Mineral. 2002;87:753–64. [CrossRef].
20. Mouhat F, Coudert FX. Necessary and sufficient elastic stability conditions in various crystal systems. Phys Rev B. 2014;90(22):224104. [CrossRef].
21. Pugh SF. XCII. Relations between the elastic moduli and the plastic properties of polycrystalline pure metals. Lond Edinb Dublin Philos Mag J Sci. 1954;45(367):823–43. [CrossRef].
22. Dadsetani M, Pourghazi A. Optical properties of strontium monochalcogenides from first principles. Phys Rev B. 2006;73(19):195102. [CrossRef].
23. Shen Y, Zhou Z. Structural, electronic, and optical properties of ferroelectric $KTa_{1/2}Nb_{1/2}O_3$ solid solutions. J Appl Phys. 2008;103(7):074113. [CrossRef].
24. Murnaghan FD. The compressibility of media under extreme pressures. Proc Nat Acad Sci U S A. 1944;30(9):244–7. [CrossRef].
25. Blanco MA, Francisco E, Luaña V. GIBBS: Isothermal-isobaric thermodynamics of solids from energy curves using a quasi-harmonic Debye model. Comput Phys Commun. 2004;158(1):57–72. [CrossRef].